**Corrected: Author Correction** 

# Bimetallic synergy in cobalt-palladium nanocatalysts for CO oxidation

Cheng Hao Wu<sup>0,1,2</sup>, Chang Liu<sup>3</sup>, Dong Su<sup>0,4</sup>, Huolin L. Xin<sup>0,4</sup>, Hai-Tao Fang<sup>2,5</sup>, Baran Eren<sup>2</sup>, Sen Zhang<sup>0,3\*</sup>, Christopher B. Murray<sup>0,6\*</sup> and Miquel B. Salmeron<sup>0,2,7\*</sup>

Bimetallic and multi-component catalysts typically exhibit composition-dependent activity and selectivity, and when optimized often outperform single-component catalysts. Here we used ambient-pressure X-ray photoelectron spectroscopy (AP-XPS) and in situ and ex situ transmission electron microscopy (TEM) to elucidate the origin of composition dependence observed in the catalytic activities of monodisperse CoPd bimetallic nanocatalysts for CO oxidation. We found that the catalysis process induced a reconstruction of the catalysts, leaving  $CoO_x$  on the nanoparticle surface. The synergy between Pd and  $CoO_x$  coexisting on the surface promotes the catalytic activity of the bimetallic catalysts. This synergistic effect can be optimized by tuning the Co/Pd ratios in the nanoparticle synthesis, and it reaches a maximum at compositions near  $Co_{0.24}Pd_{0.76}$ , which achieves complete CO conversion at the lowest temperature. Our combined AP-XPS and TEM studies provide direct observation of the surface evolution of the bimetallic nanoparticles under catalytic conditions and show how this evolution correlates with catalytic properties.

atalytic CO oxidation has been extensively studied as a model reaction<sup>1-5</sup> because of its important industrial applications in automotive exhaust treatment<sup>6,7</sup> and in fuel purification (removal of trace amounts of CO from hydrogen fuels) for proton exchange membrane fuel cells<sup>8,9</sup>. Mechanistic studies on such a model reaction and the catalysts that promote it can advance the development of catalysts for many relevant catalytic processes, such as the water–gas shift reaction and methanol oxidation<sup>5</sup>.

One strategy that has proven successful in producing efficient heterogeneous catalysts for CO oxidation is to create a synergistic interface between precious metals (for example, Pt, Au and Pd) and active metal oxide (AMO; for example, TiO2, CeO2, Co3O4 and NiO)10-15 that provides 'active' lattice oxygen to oxidize the CO adsorbed on the adjacent precious metal atoms. The lattice oxygen vacancies created in this process can bind O<sub>2</sub> and be recreated later to restart the catalytic cycle. Such an interface can be built up by loading precious metal nanoparticles onto AMO<sup>16,17</sup>, or by alloying the precious metal nanoparticles with other metals, as reported in the examples of FePt (ref. 18), FeNi (ref. 19), NiPd (ref. 20) and CuAu (ref. 21). The latter approach is appealing, as it potentially allows the interfacial effect to be realized at the atomic level over the entire nanoparticle surface. Recent advances in the colloidal synthesis of monodisperse alloy nanoparticles have enabled us to tune the bimetallic composition of nanoparticles with well defined sizes and shapes<sup>22-24</sup>.

However, bimetallic alloy nanoparticles are prone to changes during activation or reaction. These changes include reconstructions, segregation and oxidative/reductive evolution<sup>20,25-27</sup>, all of which can affect the activity and durability of the catalysts. A more precise understanding of these reaction-induced modifications is essential to elucidate the reaction mechanism and optimize the reactivity and selectivity for CO oxidation of catalysts containing bimetallic nanoparticles. Recent advances in in situ/operando

surface characterization<sup>28–32</sup> have made it possible to study catalyst surfaces and their interaction with gas-phase reactants under reaction conditions. One example is the development of AP-XPS, which makes it possible to operate this surface analysis tool under reactant gases up to Torr pressures<sup>28,33</sup> rather than under vacuum, as is traditionally required.

Herein, we combined an in situ AP-XPS investigation of monodisperse CoPd nanoparticles under CO oxidation conditions with in situ and ex situ (scanning) transmission electron microscopy ((S) TEM) and electron energy loss spectroscopy (EELS), as well as ex situ X-ray absorption spectroscopy. This integrated study reveals the surface/structure evolution and bimetallic synergy of nanoparticle catalysts in action. We observed that the atomic surface composition of CoPd alloy nanoparticles transformed during the oxidation/ reduction pretreatments. At 200 °C and 300 °C, exposure to CO drives Pd atoms to migrate to the surface, whereas O2 exposure does the opposite. Such reversible reactant-driven surface segregation, however, becomes less prominent with increasing Co content and is eventually negligible in the case of Co<sub>0.52</sub>Pd<sub>0.48</sub> nanoparticles (the nanoparticles with highest Co content), for which the surface becomes completely covered by CoO<sub>x</sub>, as corroborated by STEM-EELS mapping. The observed segregation behaviour in CoPd nanoparticles suggests that Pd and CoO<sub>x</sub> coexist on the catalyst surface, at least for nanoparticles with Co content below 50%; and such coexistence contributes to the promotion of the CO oxidation kinetics. This mechanism explains the trend of the catalytic properties of five nanoparticle catalysts of different compositions from pure Pd to Co<sub>0.52</sub>Pd<sub>0.48</sub>, among which Co<sub>0.24</sub>Pd<sub>0.76</sub> shows the lowest temperature for complete conversion of CO to CO<sub>2</sub>. This work highlights the benefits of using well defined nanoparticles as model catalysts together with in situ characterization techniques in understanding bimetallic synergy under catalytic conditions.

<sup>1</sup>Department of Chemistry, University of California, Berkeley, Berkeley, CA, USA. <sup>2</sup>Materials Science Division, Lawrence Berkeley National Laboratory, Berkeley, CA, USA. <sup>3</sup>Department of Chemistry, University of Virginia, Charlottesville, Virginia, USA. <sup>4</sup>Center for Functional Nanomaterials, Brookhaven National Laboratory, Upton, New York, USA. <sup>5</sup>School of Materials Science and Engineering, Harbin Institute of Technology, Harbin, China. <sup>6</sup>Department of Chemistry, University of Pennsylvania, Philadelphia, PA, USA. <sup>7</sup>Department of Materials Science and Engineering, University of California, Berkeley, Berkeley, CA, USA. \*e-mail: sz3t@virginia.edu; cbmurray@sas.upenn.edu; mbsalmeron@lbl.gov

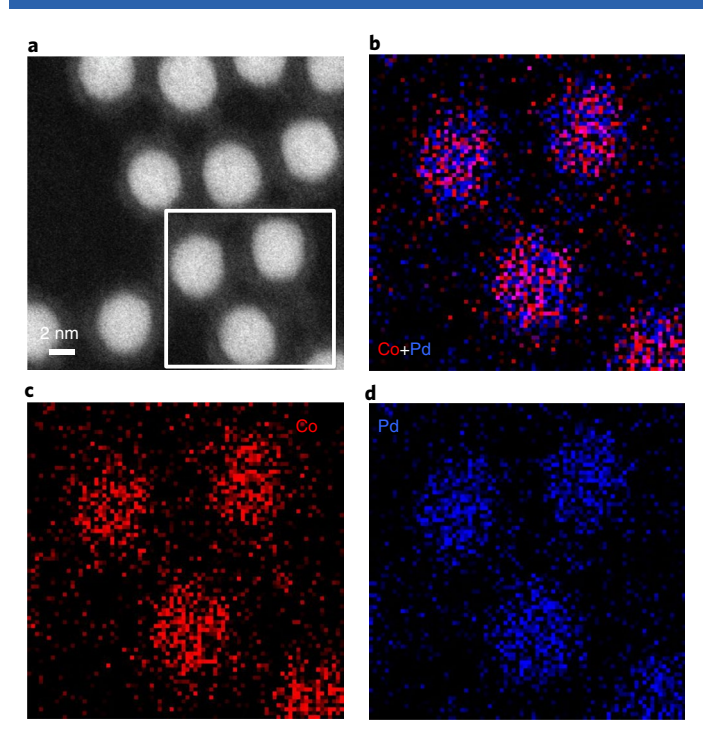


**Fig. 1 | STEM** and **EELS** elemental mapping of **4.5-nm** as-synthesized  $Co_{0.24}Pd_{0.76}$  nanoparticles. **a**, Representative dark-field STEM image of  $Co_{0.24}Pd_{0.76}$  nanoparticles. **b-d**, Overlaid Co+Pd (**b**), Co (**c**) and Pd (**d**) EELS mapping of the four nanoparticles within the white frame marked in **a**.

#### Results

Synthesis and characterization of as-synthesized Pd and CoPd nanoparticles. CoPd nanoparticles were synthesized by the co-reduction of palladium bromide (PdBr<sub>2</sub>) and cobalt acetylacetonate (Co(acac)<sub>2</sub>) in a solution of oleylamine (OAm) in the presence of tributylphosphine (TBP), as modified from a previously reported method34. OAm was used as both a solvent and a reducing agent to generate metallic alloy nanoparticles. In contrast to previous methods in which trioctylphosphine (TOP) functions as a surfactant, we used the phosphine capping agent TBP to obtain smaller nanoparticles with higher surface area, because the less bulky TBP imposes a weaker steric hindrance than TOP, allowing more nuclei to form in the nucleation process and thus leaving fewer atoms for nanoparticle growth<sup>35</sup>. As shown in the representative high-angle annular dark-field (HAADF) and bright-field TEM images in Fig. 1a and Supplementary Fig. 1b, Co<sub>0.24</sub>Pd<sub>0.76</sub> nanoparticles synthesized with TBP surfactant exhibit an average size of  $4.5 \pm 0.2$  nm, half the size of  $Co_{0.24}Pd_{0.76}$  obtained with TOP  $(9.0 \pm 0.5 \text{ nm}, \text{Supplementary Fig. 1f})$ . The composition of bimetallic alloy nanoparticles can be readily tuned by changing the molar ratio of PdBr<sub>2</sub>/Co(acac)<sub>2</sub> in the synthesis. Supplementary Fig. 1 shows TEM images of CoPd nanoparticles with various Co content, including  $Co_{0.10}Pd_{0.90}$ ,  $Co_{0.24}Pd_{0.76}$ ,  $Co_{0.38}Pd_{0.62}$  and Co<sub>0.52</sub>Pd<sub>0.48</sub>, as measured by inductively coupled plasma optical emission spectroscopy (ICP-OES). Without any post size-selection process, all nanoparticle samples are highly uniform with an average size of  $4.5 \pm 0.3$  nm. Within each nanoparticle, Co and Pd are homogeneously distributed, forming a solid solution structure, as confirmed by two-dimensional (2D) elemental mapping with aberration-corrected STEM (Fig. 1b-d). For a control experiment, 4.5-nm Pd nanoparticles were synthesized using a similar approach (Supplementary Fig. 1e). All the as-synthesized CoPd alloy nanoparticles exhibit glass-like face-centred cubic structures and weaker peaks in X-ray diffraction patterns (Supplementary Fig. 2) than Pd nanoparticles, consistent with other nanoparticles synthesized using phosphine stabilizers<sup>36</sup>.

Catalytic properties of Pd and CoPd nanoparticles in CO oxidation. Before the catalytic performance test, the as-synthesized CoPd and Pd nanoparticles were dispersed on an alumina support and then pretreated to remove the surface ligands, as described in the Methods. Alumina was chosen as the catalyst support in this study because of its relative inertness compared with titania and ceria, which allowed us to focus exclusively on the catalytic nature of the alloy nanoparticles<sup>17</sup>. In addition, the high-surface-area alumina support can protect the nanoparticles from sintering during annealing, as shown in TEM images of the catalyst before and after surface activation (Supplementary Fig. 3).

Figure 2a shows the light-off curves of CoPd and Pd nanoparticle catalysts for CO oxidation under identical testing conditions (1.0% CO, 4.0%  $\rm O_2$  in He). The incorporation of Co clearly helps to lower the temperature needed to completely oxidize CO in the gas mixture for all bimetallic nanoparticle catalysts except those with the highest Co content ( $\rm Co_{0.52}Pd_{0.48}$ ). Among the five nanoparticles,  $\rm Co_{0.24}Pd_{0.76}$  nanoparticles can achieve complete CO conversion at the lowest temperature, around 110 °C, much lower than for Pd nanoparticles (~180 °C)<sup>17</sup>. Based on the kinetic measurements (Fig. 2b), the apparent activation energy ( $\rm E_a$ ) of  $\rm Co_{0.24}Pd_{0.76}$  calculated from the corresponding Arrhenius-type plot is  $\rm 41.6\pm3.7~kJ~mol^{-1}$ , lower than the  $\rm 61.5\pm5.9~kJ~mol^{-1}$  for Pd. The catalysis test suggests that the bimetallic composition is favourable for enhanced CO oxidation kinetics and, more importantly, that Co content is crucial to optimize this enhancement.

Surface evolution of Pd and CoPd nanoparticles after pretreatments. Untreated nanoparticles showed an intense C 1s peak with weak Pd 3d or Co 3p signals because of the thick layers of organic ligands surrounding each nanoparticle. Before exposing the nanoparticles to the reactant gases, the nanoparticles were submitted to an oxidation/reduction pretreatment in the AP-XPS chamber as described in the Methods. After the pretreatment, some residual carbon was still present on the surface of nanoparticles with higher Co content (Supplementary Fig. 4), a result of the high solubility of carbon in  $\text{Co/CoO}_x$  (ref. <sup>37</sup>). Pd 3d spectra collected during the pretreatment processes showed that on the alloy nanoparticle surface, Pd was partially oxidized and reduced during oxidation/reduction cycles as expected, but Co remained oxidized, with little change noticeable in the Co 3p XPS region.

For pure Pd nanoparticles, the Pd was almost fully oxidized to PdO (at binding energy BE = 336.0 eV) after oxidation and fully reduced to metallic Pd (at BE = 335.2 eV) after reduction in  $\rm H_2$  (refs  $^{38,39}$ ), as shown in Supplementary Fig. 5. The corresponding Pd 3d spectra were used as reference spectra to determine the line shapes and fitting parameters in the subsequent analysis of all other Pd 3d spectra (more details in the Supplementary Information).

Surface evolution of Pd and CoPd nanoparticles under catalytic conditions. To understand the interactions between the nanoparticle catalyst and reactants, the pretreated CoPd nanoparticles were first exposed to 100 mTorr of O<sub>2</sub> or 100 mTorr of CO separately at different temperatures. At 300 °C, CoPd nanoparticles were exposed to 100 mTorr of CO and O<sub>2</sub> mixture with different CO/O<sub>2</sub> ratios (1:4 or 4:1). Pd 3d, Co 3p/Pd 4p and C 1s XPS spectra were monitored during these processes, with an incident photon energy of 500 eV. The photoelectrons excited from Pd 3d orbitals with 500-eV X-ray photons have kinetic energies around 160 eV, which corresponds to a probing depth of approximately 0.5 nm.

When pure Pd nanoparticles were exposed to  $100\,\mathrm{mTorr}$  of  $\mathrm{O}_2$  or CO at room temperature, the Pd 3d spectra exhibited no obvious change (Fig. 3a) except for a slight decrease (~13%) in peak intensity

ARTICLES NATURE CATALYSIS

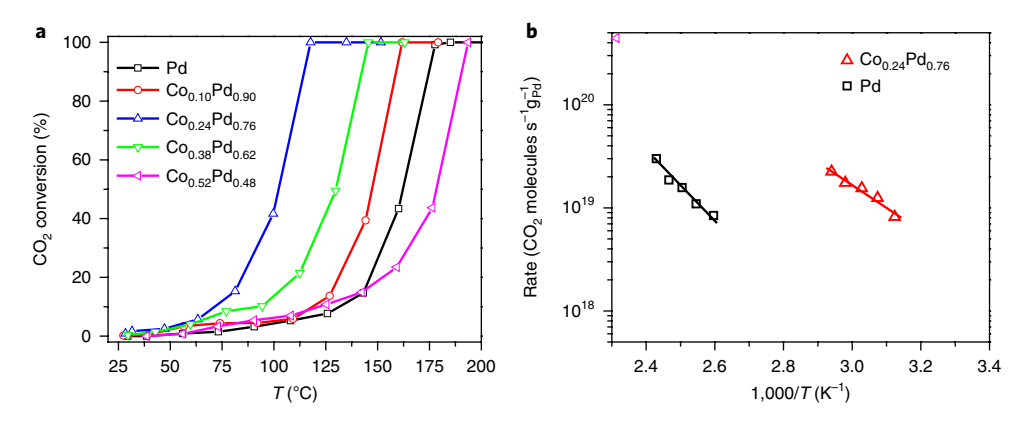


**Fig. 2 | Catalytic properties of Pd and CoPd nanoparticles. a**, Light-off curves for CO oxidation reactions on Pd nanoparticles and four CoPd alloy nanoparticles. **b**, Arrhenius plot for CO oxidation reactions over  $Co_{0.24}Pd_{0.76}$  and Pd nanoparticles.

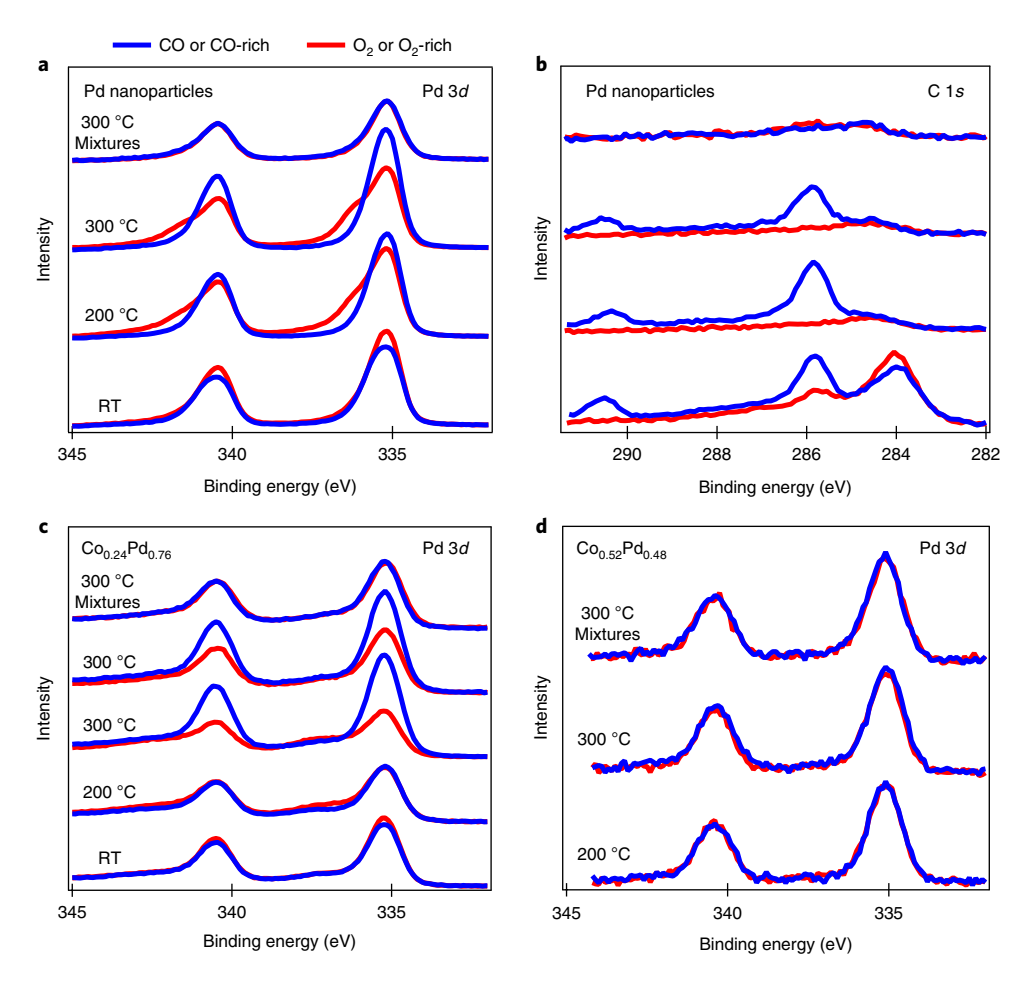


**Fig. 3 | AP-XPS** measurements on Pd and CoPd nanoparticles under reaction conditions. **a-d**, Evolution of Pd 3*d* (**a**) and C 1s (**b**) spectra for Pd nanoparticles, Pd 3*d* spectra for Pd<sub>0.24</sub>Co<sub>0.76</sub> nanoparticles (**c**), and Pd 3*d* spectra for Co<sub>0.52</sub>Pd<sub>0.48</sub> nanoparticles (**d**) under 100 mTorr of CO, O<sub>2</sub>, or mixtures of CO and O<sub>2</sub>, at different temperatures. Blue spectra were acquired under CO-only or CO-rich (4 CO:1 O<sub>2</sub>) conditions. Red spectra were acquired under O<sub>2</sub>-only or O<sub>2</sub>-rich (1 CO:4 O<sub>2</sub>) conditions. RT, room temperature.

under CO exposure. Such a decrease is likely to be due to the presence of a high coverage of adsorbed CO molecules on the surfaces, which reduces the intensity of Pd 3d signals<sup>40</sup>. The widths of the Pd  $3d_{5/2}$  peaks under both O<sub>2</sub> and CO at room temperature are slightly larger than that of the metallic Pd  $3d_{5/2}$  peak (collected after reduction in H<sub>2</sub>, as shown in Supplementary Fig. 5a) and an extra component at 0.6–0.7 eV higher BE than the metallic Pd peak was needed

to fit the overall line shape. The chemical origin of this extra component is different under CO and  $O_2$ : when exposed to CO, the BE of CO-coordinated surface Pd atoms could blueshift about  $0.6\,\mathrm{eV}$  compared with metallic Pd atoms<sup>38</sup>, whereas in  $O_2$ , Pd atoms coordinated by two O atoms (a surface sub-oxide) are responsible for the extra component<sup>38,39</sup>. C 1s spectra under CO (Fig. 3b) show three peaks at ~284, ~285.8 and ~291 eV, corresponding to residual

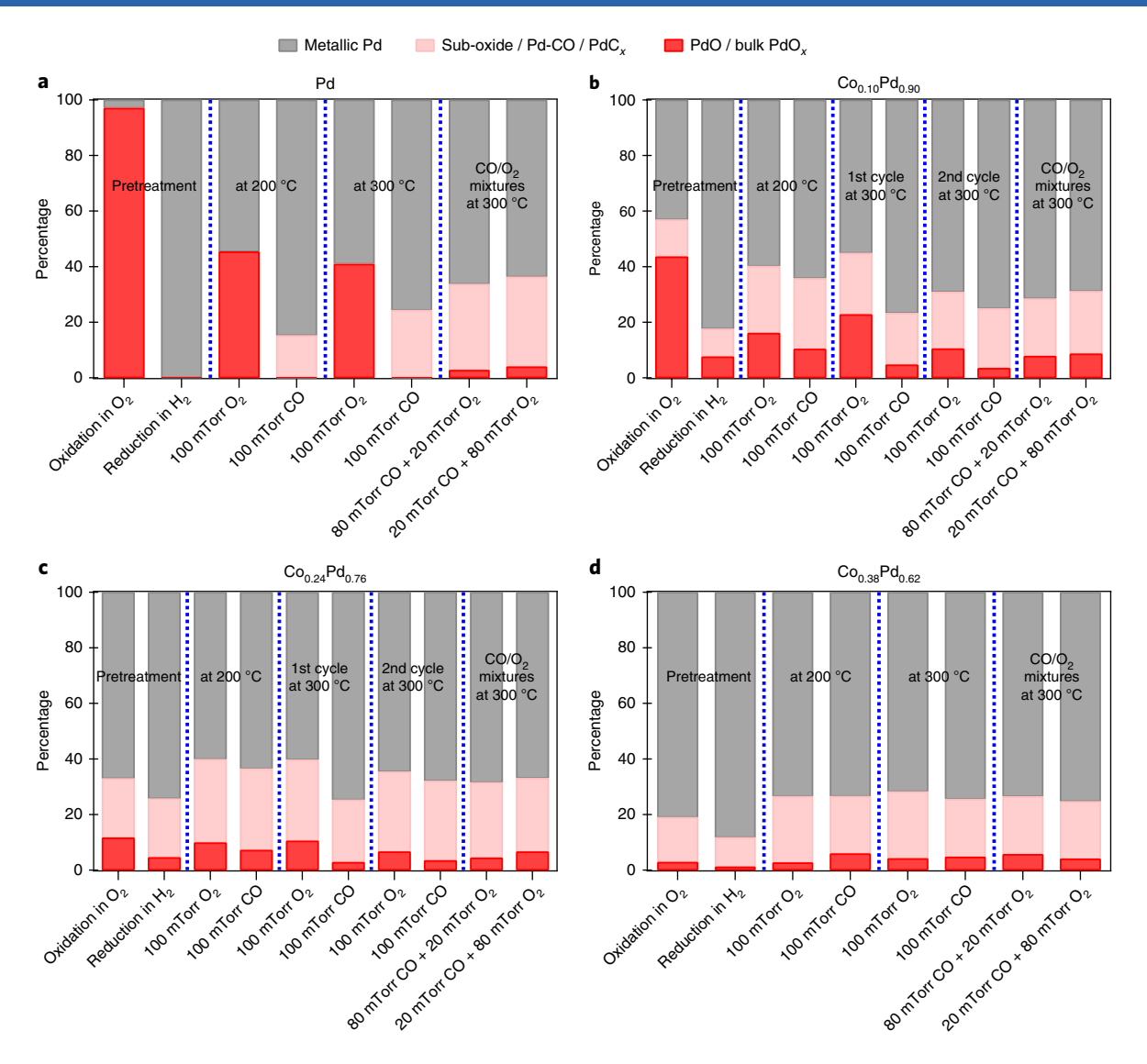


**Fig. 4 | Surface Pd speciation for Pd and CoPd nanoparticles under different conditions. a-d**, Speciation for nanoparticles of: **a**, Pd; **b**, Co<sub>0.10</sub>Pd<sub>0.90</sub>; **c**, Co<sub>0.24</sub>Pd<sub>0.76</sub>; and **d**, Co<sub>0.38</sub>Pd<sub>0.62</sub>. The percentage of each species is calculated based on peak deconvolution of the Pd 3*d* spectrum under each condition.

surface carbon species, adsorbed CO and gas-phase CO, respectively. The last two peaks disappeared on exposure to  $O_2$ , while the residual surface carbon decreased substantially.

At 200 °C and 300 °C, the Pd 3d spectra exhibited a more prominent shoulder at higher BE than metallic Pd when exposed to O<sub>2</sub>. Peak fitting (Supplementary Fig. 5) revealed the existence of substantial bulk PdO with four-fold O-coordination, with a peak centred at  $\sim\!336.0\,eV^{38,39}$ . A weak residual component above  $337\,eV$ in the  $3d_{5/2}$  region is probably related to the energy loss feature of PdO (refs 41,42) and/or a more oxidized Pd species. Under CO, adsorbed CO peaks were discernible in C1s spectra at both 200°C and 300 °C, and the Pd nanoparticle surface was more reduced. No bulk PdO was present at either temperature, but a small component at ~335.7 eV is needed to fit the overall line shape (Supplementary Fig. 5). The width of this extra component ( $\sim$ 1 eV) is consistently smaller than that of surface sub-oxide (~1.5 eV), suggesting a different origin for this component. Previous studies on CO adsorption<sup>38</sup> and decomposition<sup>43</sup> on Pd surfaces hinted that both CO-coordinated Pd (Pd-CO) and surface carbide PdC, could be responsible for the appearance of the peak at 335.7 eV, but the absence of carbide peak (~283 eV) in the C 1s spectrum rules out the presence of carbide.

When exposed to  $O_2$ -rich and CO-rich mixtures of CO and  $O_2$  at 300 °C, the Pd 3*d* spectra became indistinguishable, with the peak fitting revealing that surface Pd atoms remained mostly metallic, with a small contribution (~3%) of bulk oxide and ~30% surface sub-oxide. The evolution of the Pd species is summarized in Fig. 4a. A very weak CO gas-phase peak and an adsorbed CO peak in the C 1*s* spectra (Fig. 3b, top) indicated fast turn-over of the reactants under such conditions. The existence of surface oxides with no CO adsorption under such conditions is in line with the theoretically predicted surface phase diagram of Pd(100) under CO/O<sub>2</sub> mixtures<sup>44</sup>.

For nanoparticles with low Co content—that is,  $\mathrm{Co_{0.10}Pd_{0.90}}$  and  $\mathrm{Co_{0.24}Pd_{0.76}}$ —there was no obvious change in Pd 3d spectra at room temperature except for a small drop in intensity (~11% and ~5% respectively) under CO, as shown in Supplementary Fig. 6a and Fig. 3c. At 200 °C, a shoulder emerged under  $\mathrm{O_2}$  on the high BE side of the Pd  $3d_{5/2}$  peak, indicating oxidation of surface Pd atoms. At 300 °C the intensity of Pd 3d peaks was larger under CO than under  $\mathrm{O_2}$ , and this intensity variation was reversible, indicating reversible surface segregation of Pd depending on the gas environment. Such reversibility was corroborated by Co/Pd ratios estimated from

ARTICLES NATURE CATALYSIS

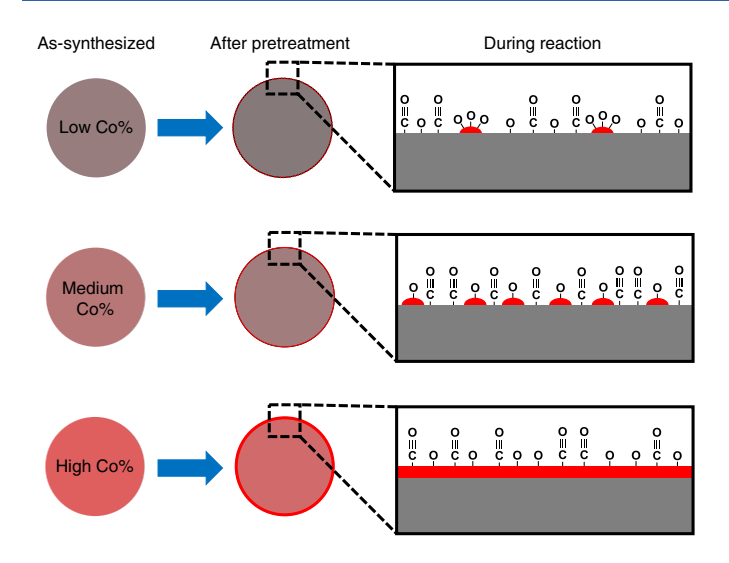


Fig. 5 | Schematic illustration of surface evolution and bimetallic synergy in CoPd alloy nanoparticles with different Co percentage content. Pd is shown in grey; Co and  $CoO_x$  are depicted in red.

the XPS peaks in the Co 3p/Pd 4p region (Supplementary Fig. 8). The surface segregation behaviour of the alloy catalysts, which was enhanced by the increased diffusion rate at elevated temperatures, can be rationalized by the lower surface energies of Pd relative to  $CoO_x$  under CO, and  $CoO_x$  relative to Pd/Pd $O_x$  under  $O_2$ . Similar segregation behaviour has been observed in several other bimetallic systems, including PdRh and PtRh nanoparticles<sup>25,26</sup>. Under the mixtures of CO and  $O_2$  (both 1:4 and 4:1 ratios) at 300 °C, there was no distinct difference in either the overall Pd 3d intensities or the surface Pd composition.

Peak deconvolution of the Pd 3d spectra revealed more details of the chemical state of the surface Pd atoms. The evolution of all relevant surface Pd species under each condition is summarized in Fig. 4b, c. Under the conditions of our experiments, the percentage of bulk-like PdO appeared to vary considerably when switching between CO and  $O_2$  at different temperatures, but the percentage of surface sub-oxide/Pd-CO remained relatively unchanged (although difficult to distinguish in peak fitting) at ~20% for  $Co_{0.10}Pd_{0.90}$  and ~30% for  $Co_{0.24}Pd_{0.76}$ . Under the different  $CO/O_2$  mixtures, the Co/Pd ratios and the chemical state of Pd were similar to those under  $O_2$ , as shown in Fig. 4b, c, and Supplementary Fig. 8. Meanwhile, the Co3p spectra showed that Costayed oxidized under all the conditions.

Given the fact that pure Pd nanoparticles can be fully reduced in H<sub>2</sub> (at 150 °C) as shown in Fig. 4a and Supplementary Fig. 5, the residual Pd sub-oxide observed in Co<sub>0.10</sub>Pd<sub>0.90</sub> is possibly a consequence of CoO<sub>x</sub> formation and its interface with surrounding Pd atoms. Unfortunately, the adsorbed CO peak was overwhelmed by the intense carbon residuals peak because of high solubility of carbon in Co/CoO<sub>x</sub> (ref. <sup>37</sup>). Moreover, our previous study on Co foils demonstrated accumulation of CoC<sub>x</sub> species under CO (ref. <sup>45</sup>). As a result, we cannot completely rule out an interaction between carbide-like carbon atoms and Pd atoms, especially at the interface between Pd and Co/CoO<sub>x</sub>. Although surface Pd sub-oxide (including Pd atoms in contact with CoO<sub>x</sub>), CO-coordinated Pd (Pd-CO) and PdC<sub>x</sub> may coexist on the surface, their Pd 3d peaks are very close and thus difficult to distinguish in the fitting process. For that reason, they were represented by one single component in the peak deconvolution of all the Pd 3d spectra of alloy nanoparticles.

For samples with relatively high Co content—that is,  $Co_{0.38}Pd_{0.22}$  and  $Co_{0.52}Pd_{0.48}$ —the signal-to-noise ratios of the Pd3d spectra (Supplementary Fig. 6b and Fig. 3d) became noticeably worse, while

the Co 3*p* signal was substantially more intense (Supplementary Fig. 7b) in the Co 3*p*/Pd 4*p* region. Unlike the cases of Co<sub>0.10</sub>Pd<sub>0.90</sub> and Co<sub>0.24</sub>Pd<sub>0.76</sub>, under all the tested conditions neither the intensity nor the line shape of the Pd 3*d* and Co 3*p*/Pd 4*p* peak exhibited large variations. Although the noisier Pd 3*d* and Pd 4*p* signals potentially brought larger errors into the fitting process, tentative fitting results on Co<sub>0.38</sub>Pd<sub>0.22</sub> also suggested smaller variations in the surface compositions (both Co/Pd ratios and percentages of Pd species) under all the conditions tested, as shown in Fig. 4d and Supplementary Fig. 8. Co 2*p* XPS spectra would be useful to further analyse the chemical states of the surface Co species. Unfortunately, the photon flux and energy resolution above 750 eV at the beamline used here prevented us from acquiring meaningful Co 2*p* spectra, especially under in situ conditions.

In situ EELS and ex situ XAS characterization. To look closely at the chemical states of Co in the alloy nanoparticles, we carried out STEM/EELS measurements on CoPd nanoparticles under conditions similar to the AP-XPS experiments using an environmental TEM. Co L-edge EELS spectra collected after heating in CO/O<sub>2</sub> mixtures for 40 min at 200 °C exhibited an L<sub>3</sub>/L<sub>2</sub> ratio of ~3.8, lower than that under reducing environments (~5.0-5.2 after H<sub>2</sub> pretreatment or under CO only; shown in Supplementary Fig. 9). The L<sub>3</sub>/L<sub>2</sub> ratio in the EELS spectra is reported to be an indicator of the oxidation states of 3d transition metals<sup>46,47</sup>. The measured L<sub>3</sub>/L<sub>2</sub> ratios suggested mostly Co(II) under reducing environment in H2 or CO and a mixture of Co(II)/Co(III) in the mixture of CO/O2. Ex situ X-ray absorption spectroscopy (XAS) measurements on the postreaction nanoparticles also suggested complete oxidation of Co. As illustrated in Supplementary Fig. 10, the bulk-sensitive partial fluorescence yield (PFY) XAS spectra of all four alloy nanoparticles shows dominating Co(III) characteristics, whereas the surfacesensitive total electron yield (TEY) XAS spectra showed substantial Co(II) species on the surface.

Composition-dependent bimetallic synergy. The aforementioned activity test showed a clear correlation between the composition of CoPd nanoparticles and their catalytic activity for CO oxidation. Based on the surface evolution observed in both spectroscopic and microscopic characterizations, we propose a mechanism for the synergy of bimetallic CoPd nanoparticles as shown in Fig. 5, which illustrates the composition-dependent structure change of CoPd nanoparticles under CO oxidation conditions.

Pd and Co are uniformly distributed in the as-synthesized alloy nanoparticles, as evidenced by STEM-EELS elemental mapping in Fig. 1 and Supplementary Fig. 1. After pretreatment to remove surfactants, Co is segregated to the surface of nanoparticles as an oxide. Heating in H<sub>2</sub> at 150 °C partially reduces Pd on the surface, but the temperature is not sufficient to reduce the CoO<sub>x</sub> to Co metal<sup>45</sup>. It is clear that a large Co content in the nanoparticles would produce a surface CoO<sub>x</sub> layer that would completely cover the Pd core, as shown by ex situ STEM image and EELS mapping (Supplementary Fig. 11) of pretreated Co<sub>0.52</sub>Pd<sub>0.48</sub> nanoparticles. Low Co content on the other hand would produce a partial coverage on the surface, exposing metallic Pd and creating a substantial amount of boundaries and interfaces between Pd and CoO, which are prime candidates for sites where the CO oxidation is enhanced. For the 4.5-nm nanoparticles used here, the composition that would produce one complete monolayer of CoO, if completely segregated to the surface, can be estimated as being around 20% (see Supplementary Information), close to the experimental composition of Co<sub>0.24</sub>Pd<sub>0.76</sub> that produces the best catalyst.

The strong adsorption of CO on metallic Pd, together with the high oxygen affinity of Co, drives the surface composition changes, with segregation of Co under  $\rm O_2$  and Pd under CO. In addition to the increased island perimeter at low Co content where O atoms

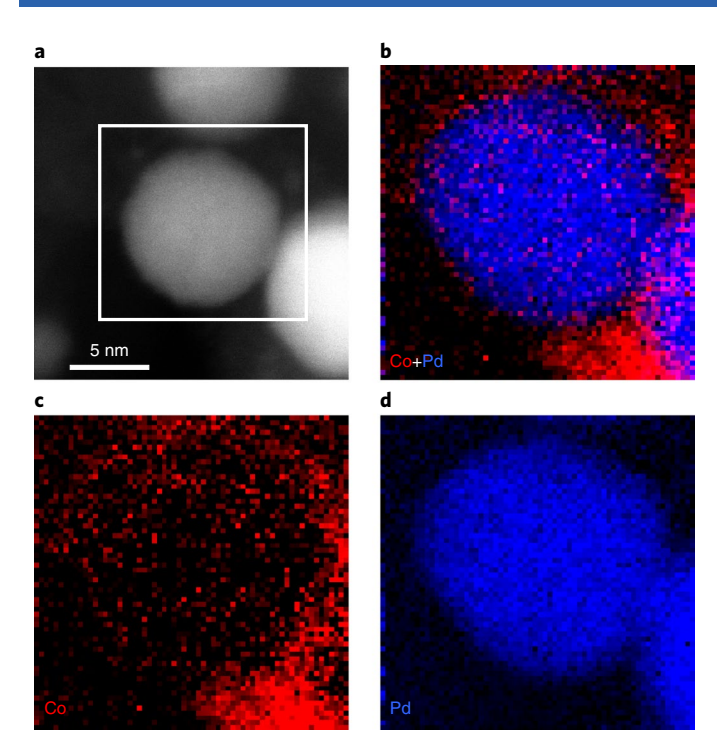


**Fig. 6 | STEM** and **EELS** elemental mapping of 10-nm  $Co_{0.24}Pd_{0.76}$  nanoparticles after pretreatment. **a**, Representative dark-field STEM image of  $Co_{0.24}Pd_{0.76}$  nanoparticles. **b-d**, Overlaid Co+Pd (**b**), Co (**c**), and Pd (**d**) EELS mapping of the four nanoparticles within the white frame marked in **a**.

from CoO, can migrate and react with a CO molecule on neighbouring Pd atoms to form a CO2 molecule, CO may also react with O atoms on the Pd-supported CoO, monolayer, producing O-vacancies and thus activating Co for CO adsorption and reaction with lattice O. These two effects are maximized at CoO<sub>x</sub> coverages near or below one monolayer, which is expected to occur near the optimal composition determined in our catalytic CO oxidation studies. Unfortunately, imaging a monolayer-thickness CoO, shell on a 4.5-nm nanoparticle surface is challenging in STEM, and we were not able to obtain conclusive images of monolayer shells, except for small CoO<sub>x</sub> clusters occasionally spotted on the nanoparticle surface, as shown in the STEM image and EELS mapping in Supplementary Fig. 12. However, larger particles with the same composition produce thicker shells, easier to observe in STEM, as shown for the 10-nm Co<sub>0.24</sub>Pd<sub>0.76</sub> nanoparticles in Fig. 6, in which a thin Co shell covering the Pd core is visible, thus corroborating the Co segregation behaviour deduced from the AP-XPS results.

At higher Co content, the segregated CoO<sub>x</sub> species eventually form a thick continuous shell covering the entire Pd core, as clearly demonstrated in the case of Co<sub>0.52</sub>Pd<sub>0.48</sub> (Supplementary Fig. 11). The deeper buried Pd core is thus isolated from the gas reactants, and the CoO<sub>x</sub> shell is solely responsible for the CO oxidation, which proves to be a worse catalyst for CO oxidation than pure Pd. One can imagine that a higher reduction temperature may help to further reduce CoO<sub>x</sub> back to its metallic phase, resulting in the formation of a PdCo alloy again. With coexistence of both elements on the surface, the synergetic effect should become prominent again. Indeed, a control experiment in which the Co<sub>0.52</sub>Pd<sub>0.48</sub> nanoparticles were treated in H<sub>2</sub> (5.0% in He) at 400 °C supports this hypothesis. As shown in Fig. 7, the resulting alloy nanoparticles initially showed much enhanced catalytic activity as the reduced Co alloying into the nanoparticle restored the optimal ratio of CoO<sub>x</sub>-Pd and boundary or interface sites, but became rapidly deactivated above 150 °C, because of re-segregation and oxidation of the Co on the surface.

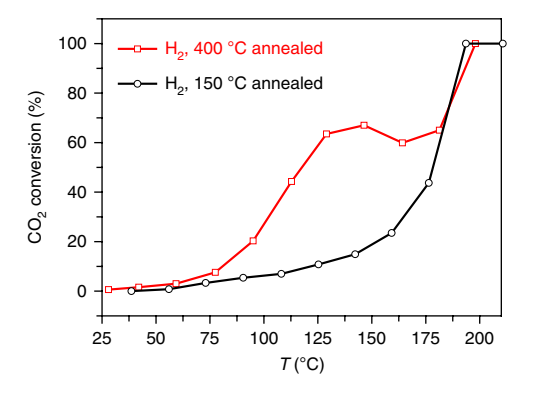


Fig. 7 | The impact of pretreatment temperature on the activity of  $Co_{0.52}Pd_{0.48}$  nanoparticles. CO oxidation light-off curves of  $Co_{0.52}Pd_{0.48}$  nanoparticles that underwent  $H_2$  pretreatment at 150 °C (black circles) and 400 °C (red squares).

The proposed mechanism for synergetic effect of CoPd nanoparticles explains why an optimal Co composition exists for the catalytic CO oxidation reaction, in which the Co segregation and oxidation on the surface play an important role. Similar segregation behaviours were also observed on several surface alloys such as PdSn and PtSn, where Sn segregates to the surface under oxidative conditions and forms thin layers of SnO<sub>x</sub> that wet the entire alloy surface 48,49. Moreover, these thin oxide overlayers were found to be substantially less thermally stable than their bulk counterpart 48,49, which makes them more likely to participate in catalytic cycles involving oxygen. It is possible that such bimetallic synergy originating from selective segregation is responsible for many examples of composition-dependent catalytic activity reported in the literature.

# Conclusion

In conclusion, we used AP-XPS and other complementary characterization techniques to investigate the surface evolution of a series of CoPd alloy nanoparticles under CO oxidation reactions and revealed the origin of the composition dependence of their catalytic activity. We found that under reaction conditions, Co segregated to the surface as an oxide after pretreatment. Exposure to CO at elevated temperatures drove more Pd to migrate to the surface, whereas O<sub>2</sub> exposure did the opposite. The variation in surface composition under CO or O<sub>2</sub> became less prominent with increasing Co content, because of increasing CoO<sub>x</sub> coverage. The correlation between catalytic performance and surface composition indicates that coexisting Pd and CoO<sub>x</sub> on the surface provides the sites that are responsible for promoting CO oxidation kinetics. We anticipate that the composition-dependent surface segregation behaviour and synergistic effect play essential roles in many other bimetallic catalyst systems. Our study illustrates that the use of advanced in situ characterization techniques can assist in understanding relevant surface phenomena and provide meaningful guidance for the design and optimization of bimetallic and multi-component catalysts.

### Methods

Chemicals and materials. Oleylamine (OAm, >70%), tributylphosphine (TBP, 97%), trioctylphosphine (TOP, 97%), palladium bromide (PdBr<sub>2</sub>, 99%), palladium aceylacetonate (Pd(acac)<sub>2</sub>, 99%) and cobalt acetylacetonate (Co(acac)<sub>2</sub>, 97%) were all purchased from Sigma Aldrich and used without further purification. Hexane, isopropanol and acetone were all purchased from Fisher Scientific and used without further purification. Alumina was purchased from Sasol (TH100/150) and calcined at 900 °C for 24 hours for further usage.

Synthesis of Pd and CoPd alloy nanoparticles. In a typical synthesis of  $Co_{0.24}Pd_{0.76}$  nanoparticles, 52 mg of  $Co(acac)_2$  and 81 mg of  $PdBr_2$  was mixed with 18 ml of OAm and 0.25 ml of TBP under stirring. The mixture was heated to 85 °C for 1 hour under vacuum to generate a brown transparent solution with the impurities

ARTICLES NATURE CATALYSIS

and moistures removed, and then protected with  $N_2.$  The solution was further heated to 260 °C at a rate of 5 °C min  $^{-1}$  and kept at this temperature for 2 hours before cooling to room temperature. The nanoparticles were separated by adding 50 ml of isopropanol into the mixture, followed by centrifugation (8,500 r.p.m., 8 min). They were further purified through cycles of dispersing (adding hexane), precipitation (adding isopropanol) and centrifugation, and then stored in hexane under ambient conditions.

Using the same conditions, simply varying the amounts of Co precursor to 26 mg, 78 mg and 104 mg of  $Co(acac)_2$  can yield  $Co_{0.10}Pd_{0.90}$ ,  $Co_{0.38}Pd_{0.62}$  and  $Co_{0.52}Pd_{0.48}$ , respectively. To obtain Pd nanoparticles, 90 mg of Pd(acac)\_2 instead of PdBr<sub>2</sub> was used in the above synthetic procedure without adding  $Co(acac)_2$  precursor.

Catalyst loading, activation and catalysis evaluation. An appropriate amount of nanoparticles dissolved in hexane was added to a dispersion of  $Al_2O_3$  in 15 ml of hexane (to obtain a final metal loading of 0.5 wt% verified by ICP-OES) and was stirred for 3 hours to allow the nanoparticles to be completely absorbed onto  $Al_2O_3$ . The composite of nanoparticles and  $Al_2O_3$  was collected by centrifugation and washed with acetone. The solid powder was dried under vacuum overnight and then annealed in air at 300 °C for 3 hours to completely remove the organic surfactants.

The catalyst was sieved below 150 µm of grain size and then put into the reactor quartz tube (inner diameter 3.8 mm) and immobilized with two layers of quartz wool to prevent displacement of the catalyst powder. Before CO oxidation catalysis testing, the catalyst was activated through mild reduction at 150 °C for 30 mins in the presence of  $\rm H_2$  (5%  $\rm H_2$  in the He). CO oxidation was performed under an oxidative gas condition at atmospheric pressure. We used a mixed gas of CO,  $\rm O_2$  and He (1.0% CO, 4.0%  $\rm O_2$ ) with a constant flow rate of 30 ml min $^{-1}$  and a gas hourly space velocity of 60,000 ml g $^{-1}$  h $^{-1}$ . For light-off curve experiments, the reactant mixture was heated to the desired temperature with a ramping rate of 3 °C min $^{-1}$ . The composition of the effluent gases was monitored on-line using a gas chromatograph (Buck Scientific 910) equipped with a thermal conductivity detector, using He as the carrier gas.

AP-XPS. Measurements were carried out at the beamline 9.3.2 of the Advanced Light Source at Lawrence Berkeley National Laboratory. Before the experiment session started, the measurement chamber was baked at 120 °C for more than 24 hours, and the base pressure in the measurement chamber reached low  $10^{-9} {\rm Torr}.$  Before the introduction of CO into the measurement chamber, the CO gas (99.99% purity) was passed through a hot trap of copper beads at 250 °C, to remove any carbonyl contaminants. Similarly, ultra-pure  ${\rm H_2}$  gas (99.99% purity) was passed through a liquid nitrogen trap to minimize residual water impurities by freezing.

Because the insulating nature of the alumina support that we used in the catalytic performance test can induce severe charging effects during XPS measurements, the nanoparticles were instead drop-cast on a piece of silicon substrate for AP-XPS measurements. The native oxide layer on the silicon surface served as a substitute for inert oxide support for the catalysts.

Because of the limitation on pressures in the AP-XPS system, the pretreatment procedures of the nanoparticle sample were modified accordingly. The modified pretreatment procedure involves a few cycles of oxidation/reduction, until the carbon composition in the XPS spectra stays mostly unchanged between two consecutive reduction cycles. Each oxidation step was performed under 500 mTorr  $O_2$  at 300 °C for 20 minutes, and each reduction step under 200 mTorr  $H_2$  at 150 °C for 20 minutes. C1s XPS spectra were continuously monitored during the pretreatment. After completing each oxidation/reduction step, XPS spectra in Pd 3d, Co 3p/Pd 4p and C 1s regions were also collected.

The procedure of spectral analysis, including energy calibration and peak deconvolution, is described in detail in the Supplementary Methods.

(S)TEM and EELS characterization. High-resolution ex situ STEM analyses on CoPd nanoparticles were carried out using a Hitachi HD2700C (200 kV) with a probe aberration corrector, in the Center for Functional Nanomaterials at Brookhaven National Lab. The EELS spectra and mapping were collected using a high-resolution Gatan-Enfina ER with a probe size of 1.3 Å, typical probe current of 80-100 pA and a dwell time of 0.07 s at binning of 100. A power-law function was used for EELS background subtraction. For as-synthesized Co<sub>x</sub>Pd<sub>1</sub> alloy nanoparticles, samples were prepared by depositing a single drop of diluted nanoparticle dispersion in hexane on an ultrathin holey carbon film (<3 nm) supported on a copper grid. For pretreated Co<sub>0.52</sub>Pd<sub>0.48</sub> nanoparticles, Co<sub>0.52</sub>Pd<sub>0.48</sub> were loaded onto carbon (Vulcan-72, Fuel Cell Stores) with a nanoparticle/carbon weight ratio of 1:1 and then annealed in air at 300 °C for 3 hours to completely remove the organic surfactants. The pretreated  $Co_{0.52}Pd_{0.48}$  nanoparticles supported on carbon were dispersed in acetone and transferred to an ultrathin holey carbon film supported on a copper grid for STEM characterization. We use carbon to replace Al<sub>2</sub>O<sub>3</sub> here because Al<sub>2</sub>O<sub>3</sub> is subject to charge accumulation under highenergy electron beam, making 2D EELS mapping insurmountably challenging.

Environmental (S)TEM study of CoPd nanoparticles was performed in a FEI Environmental Titan operated at 300 keV. This instrument is equipped with a differential pumping system, a Schottky field-emission gun, an objective-lens

aberration corrector, a Gatan Tredium electron energy loss spectrometer, and a gas manifold that can mix and flow four different gas streams. Under heating conditions, CO is prone to decompose under the high-energy electron beam and causes carbon contamination to the catalysts. To avoid that, we collected in situ EELS spectra in the TEM mode to spread the dose.

Other structure and composition characterizations. X-ray powder diffraction patterns were obtained on a Rigaku Smartlab diffractometer with Cu K $\alpha$  radiation ( $\lambda$ = 1.5418 Å). Quantitative elemental analyses for the composition of nanoparticles were carried out with inductively coupled plasma–optical emission spectrometry (ICP-OES) on a SPECTRO GENESIS ICP spectrometer. TEM images were obtained using a JEOL 1400 (120 kV).

Ex situ X-ray absorption measurements was carried out at beamline 6.3.1.2 of the Advanced Light Source. PFY signal was collected with a Vortex silicon drift detector. TEY signal was measured as the drain current from the sample via an SRS 570 amplifier. All spectra were normalized by photon flux, represented by the TEY current measured from a gold mesh in the X-ray pipeline.

## Data availability

The data that support the plots within this paper and other findings of this study are available from the corresponding author upon reasonable request.

Received: 14 February 2018; Accepted: 31 October 2018; Published online: 10 December 2018

#### References

- Dyakonov, A. & Robinson, E. Low-temperature oxidation of CO in smoke: a review. Beitr. Tabakforsch. 22, 88–106 (2006).
- van Spronsen, M. A., Frenken, J. W. M. & Groot, I. M. N. Surface science under reaction conditions: CO oxidation on Pt and Pd model catalysts. Chem. Soc. Rev. 46, 4347–4374 (2017).
- Imbihl, R. Oscillatory reactions on single crystal surfaces. Prog. Surf. Sci. 44, 185–343 (1993).
- Rodriguez, J. A. & Goodman, D. W. High-pressure catalytic reactions over single-crystal metal-surfaces. Surf. Sci. Rep. 14, 1–107 (1991).
- Freund, H. J., Meijer, G., Scheffler, M., Schlögl, R. & Wolf, M. CO oxidation as a prototypical reaction for heterogeneous processes. *Angew. Chem. Int. Ed.* 50, 10064–10094 (2011).
- Heck, R. M. & Farrauto, R. J. Automobile exhaust catalysts. *Appl. Catal. A* 221, 443–457 (2001).
- Twigg, M. V. Progress and future challenges in controlling automotive exhaust gas emissions. Appl. Catal. B 70, 2–15 (2007).
- Nilekar, A. U., Alayoglu, S., Eichhorn, B. & Mavrikakis, M. Preferential CO oxidation in hydrogen: reactivity of core-shell nanoparticles. *J. Am. Chem.* Soc. 132, 7418–7428 (2010).
- Fu, Q. et al. Interface-confined ferrous centers for catalytic oxidation. Science 328, 1141–1144 (2010).
- Saavedra, J., Doan, Ha, Pursell, C. J., Grabow, L. C. & Chandler, B. D. The critical role of water at the gold-titania interface in catalytic CO oxidation. *Science* 345, 1599–1602 (2014).
- 11. Wang, Y. G., Yoon, Y., Glezakou, V. A., Li, J. & Rousseau, R. The role of reducible oxide-metal cluster charge transfer in catalytic processes: new insights on the catalytic mechanism of CO oxidation on Au/TiO<sub>2</sub> from ab initio molecular dynamics. J. Am. Chem. Soc. 135, 10673–10683 (2013).
- Kim, H. Y., Lee, H. M. & Henkelman, G. CO oxidation mechanism on CeO<sub>3</sub>-supported Au nanoparticles. J. Am. Chem. Soc. 134, 1560–1570 (2012).
- Widmann, D. & Behm, R. J. Active oxygen on a Au/TiO<sub>2</sub> catalyst: formation, stability, and CO oxidation activity. *Angew. Chem. Int. Ed.* 50, 10241–10245 (2011).
- Haruta, M., Kobayashi, T., Sano, H. & Yamada, N. Novel gold catalysts for the oxidation of carbon monoxide at a temperature far below 0°C. *Chem. Lett.* 16. 405–408 (1987).
- Wang, C., Yin, H., Dai, S. & Sun, S. A general approach to noble metal—metal oxide dumbbell nanoparticles and their catalytic application for CO oxidation. *Chem. Mater.* 22, 3277–3282 (2010).
- An, K. et al. Enhanced CO oxidation rates at the interface of mesoporous oxides and Pt nanoparticles. J. Am. Chem. Soc. 135, 16689–16696 (2013).
- Cargnello, M. et al. Control of metal nanocrystal size reveals metal-support interface role for ceria catalysts. Science 341, 771–773 (2013).
- Zhu, H. et al. Constructing hierarchical interfaces: TiO<sub>2</sub>-supported PtFe-FeO<sub>x</sub> nanowires for room temperature CO oxidation. J. Am. Chem. Soc. 137, 10156–10159 (2015).
- 19. Chen, G. et al. Interfacial effects in iron–nickel hydroxide–platinum nanoparticles enhance catalytic oxidation. *Science* **344**, 495–499 (2014).
- Shan, S. et al. Atomic-structural synergy for catalytic CO oxidation over palladium-nickel nanoalloys. J. Am. Chem. Soc. 136, 7140–7151 (2014).
- Zhan, W. et al. Crystal structural effect of AuCu alloy nanoparticles on catalytic CO oxidation. J. Am. Chem. Soc. 139, 8846–8854 (2017).

- Gilroy, K. D., Ruditskiy, A., Peng, H.-C., Qin, D. & Xia, Y. Bimetallic nanocrystals: syntheses, properties, and applications. *Chem. Rev.* 116, 10414–10472 (2016).
- Yu, W., Porosoff, M. D. & Chen, J. G. Review of Pt-based bimetallic catalysis: from model surfaces to supported catalysts. *Chem. Rev.* 112, 5780–5817 (2012).
- Guo, S., Zhang, S. & Sun, S. Tuning nanoparticle catalysis for the oxygen reduction reaction. *Angew. Chem. Int. Ed.* 52, 8526–8544 (2013).
- Tao, F. et al. Reaction-driven restructuring of Rh–Pd and Pt–Pd core–shell nanoparticles. Science 322, 932–934 (2008).
- Tao, F. et al. Evolution of structure and chemistry of bimetallic nanoparticle catalysts under reaction conditions. J. Am. Chem. Soc. 132, 8697–8703 (2010).
- Carenco, S. et al. Dealloying of cobalt from CuCo nanoparticles under syngas exposure. J. Phys. Chem. C 117, 6259–6266 (2013).
- Ogletree, D. F. et al. A differentially pumped electrostatic lens system for photoemission studies in the millibar range. Rev. Sci. Instrum. 73, 3872 (2002).
- Wu, C. H., Weatherup, R. S. & Salmeron, M. B. Probing electrode/electrolyte interfaces in situ by X-ray spectroscopies: old methods, new tricks. *Phys. Chem. Chem. Phys.* 17, 30229–30239 (2015).
- Zheng, H., Meng, Y. S. & Zhu, Y. Frontiers of in situ electron microscopy. MRS Bull. 40, 12–18 (2015).
- Escudero, C. et al. A reaction cell with sample laser heating for in situ soft X-ray absorption spectroscopy studies under environmental conditions. J. Synch. Radiat. 20, 504–508 (2013).
- 32. Heine, C. et al. Ambient-pressure soft X-ray absorption spectroscopy of a catalyst surface in action: closing the pressure gap in the selective n-butane oxidation over vanadyl pyrophosphate. J. Phys. Chem. C 118, 20405–20412 (2014).
- Bluhm, H., Ogletree, D. F., Fadley, C. S., Hussain, Z. & Salmeron, M. The premelting of ice studied with photoelectron spectroscopy. *J. Phys. Condens. Matter.* 14, L227–L233 (2002).
- Sun, D., Mazumder, V., Metin, O. & Sun, S. Catalytic hydrolysis of ammonia borane via cobalt palladium nanoparticles. ACS Nano 5, 6458–6464 (2011).
- Sun, S. & Murray, C. B. Synthesis of monodisperse cobalt nanocrystals and their assembly into magnetic superlattices (invited). *J. Appl. Phys.* 85, 4325–4330 (1999).
- Zhang, S. et al. Monodisperse core/shell Ni/FePt nanoparticles and their conversion to Ni/Pt to catalyze oxygen reduction. J. Am. Chem. Soc. 136, 15921–15924 (2014).
- 37. Ishida, K. & Nishizawa, T. The C-Co (carbon-cobalt) system. *J. Phase Equilibria* 12, 417–424 (1991).
- Toyoshima, R. et al. Active surface oxygen for catalytic CO oxidation on Pd(100) proceeding under near ambient pressure conditions. J. Phys. Chem. Lett. 3, 3182–3187 (2012).
- 39. Ketteler, G. et al. In situ spectroscopic study of the oxidation and reduction of Pd(111). *J. Am. Chem. Soc.* **127**, 18269–18273 (2005).
- Gries, W. H. Angular intensity modulation in angle-resolved XPS and AES of non-crystalline ultrathin surface layers: the phenomenon and its implications. Surf. Interface Anal. 17, 803–812 (1991).
- Kibis, L. S., Titkov, A. I., Stadnichenko, A. I., Koscheev, S. V. & Boronin, A. I. X-ray photoelectron spectroscopy study of Pd oxidation by RF discharge in oxygen. *Appl. Surf. Sci.* 255, 9248–9254 (2009).
- Militello, M. C. Palladium oxide (PdO) by XPS. Surf. Sci. Spectra 3, 395 (1994).

- 43. Balmes, O. et al. Reversible formation of a PdC<sub>x</sub> phase in Pd nanoparticles upon CO and O<sub>2</sub> exposure. *Phys. Chem. Chem. Phys.* **14**, 4796 (2012).
- 44. Rogal, J., Reuter, K. & Scheffler, M. Oxidation at Pd(100): a first-principles constrained thermodynamics study. *Phys. Rev. B* 75, 1–11 (2007).
- Wu, C. H., Eren, B., Bluhm, H. & Salmeron, M. B. Ambient-pressure X-ray photoelectron spectroscopy study of cobalt foil model catalyst under CO, H<sub>2</sub>, and their mixtures. ACS Catal. 7, 1150–1157 (2017).
- Wang, Z. L., Bentley, J. & Evans, N. D. Valence state mapping of cobalt and manganese using near-edge fine structures. *Micron* 31, 355–362 (2000).
- Wang, Z. L., Yin, J. S. & Jiang, Y. D. EELS analysis of cation valence states and oxygen vacancies in magnetic oxides. *Micron* 31, 571–580 (2000).
- 48. Lee, A. F. & Lambert, R. M. Oxidation of Sn overlayers and the structure and stability of Sn oxide films on Pd(111). *Phys. Rev. B* **58**, 4156–4165 (1998).
- Batzill, M., Beck, D. E., Jerdev, D. & Koel, B. E. Tin-oxide overlayer formation by oxidation of Pt-Sn(111) surface alloys. *J. Vac. Sci. Technol. A* 19, 1953 (2001).

# Acknowledgements

This work was supported by the Office of Basic Energy Sciences of the US Department of Energy under contract no. DE-AC02-05CH11231 through the Chemical Sciences, Geosciences, and Biosciences Division. Funding from the same contract for the ALS and beamline 9.3.2 is also acknowledged. Partial work on CoPd nanoparticles synthesis and characterization were supported by US National Science Foundation (DMR-1809700) and Jeffress Trust Awards Program in Interdisciplinary Research from Thomas E. and Kate Miller Jeffress Memorial Trust. Partial work on electron microscopy carried out at the Center for Functional Nanomaterials, Brookhaven National Laboratory, was supported by the US Department of Energy, Office of Basic Energy Sciences, under contract no. DE-AC02-98CH10886.

# **Author Contributions**

The project was conceived by C.H.W. and C.L. under the supervision of S.Z, M.B.S. and C.B.M. Catalyst synthesis, basic characterization and catalytic activity measurements were performed by C.L. and S.Z. AP-XPS experiments were conducted by C.H.W., H.-T.F. and B.E. Ex situ TEM and elemental mapping were done by D.S. In situ TEM and EELS measurements were performed by H.X., C.H.W. and S.Z. Ex situ XAS measurements were done by C.H.W. The analysis and interpretation of all spectra (XPS, XAS and EELS) were done by C.H.W. All authors contributed to the writing of the manuscript.

## Competing interests

The authors declare no competing interests.

# **Additional information**

**Supplementary information** is available for this paper at https://doi.org/10.1038/s41929-018-0190-6.

Reprints and permissions information is available at www.nature.com/reprints.

Correspondence and requests for materials should be addressed to S.Z. or C.B.M. or M.B.S.

**Publisher's note:** Springer Nature remains neutral with regard to jurisdictional claims in published maps and institutional affiliations.

© The Author(s), under exclusive licence to Springer Nature Limited 2018